



Article

# High-Q Resonances Enabled by Bound States in the Continuum for a Dual-Parameter Optical Sensing

Hongshun Liu<sup>1</sup>, Yuntao Pan<sup>1</sup>, Hongjian Lu<sup>1</sup>, Zongyu Chen<sup>1</sup>, Xuguang Huang<sup>1</sup> and Changyuan Yu<sup>1,2,\*</sup>

- JinjiangTechnology and Innovation Research Institute, The Hong Kong Polytechnic University, Quanzhou 362216, China; hsliu@hkpolyu-jjresearch.cn (H.L.); ytpan@polyu.edu.hk (Y.P.); hong-jian.lu@connect.polyu.hk (H.L.); zongyu.chen@hkpolyu-jjresearch.cn (Z.C.); xghuang@hkpolyu-jjresearch.cn (X.H.)
- Photonics Research Institute, Department of Electrical and Electronic Engineering, The Hong Kong Polytechnic University, Hong Kong 999077, China
- \* Correspondence: changyuan.yu@polyu.edu.hk

Abstract: Optical sensing technologies, particularly refractive index and temperature sensing, are pivotal in biomedical, environmental, and industrial applications. This study introduces a dual-parameter all-dielectric transmissive grating sensor leveraging symmetryprotected bound states in the continuum (BICs). A one-dimensional silicon grating on a silica substrate was designed and analyzed using finite element analysis software. The proposed grating structure enables the excitation of two distinct BICs, both exhibiting high quality factors (Q-factors) of  $Q_{\rm I}=8.03\times10^4$  for Mode I and  $Q_{\rm II}=4.48\times10^4$ for Mode II. These modes demonstrate significantly different sensing characteristics due to their unique field distributions: Mode I predominantly confines its electromagnetic field within the grating slits, achieving an outstanding refractive index (RI) sensitivity of  $S_{\rm RI}^{\rm I} = 406 \, \rm nm/RIU$  with a minor thermal sensitivity of  $S_{\rm T}^{\rm I} = 0.052 \, \rm nm/^{\circ} C$ . In contrast, Mode II concentrates its field energy in the silicon substrate, resulting in enhanced thermal sensitivity of  $S_T^{II} = 0.078 \text{ nm}/^{\circ}\text{C}$  while maintaining a refractive index sensitivity of  $S_{RI}^{II} = 220 \text{ nm/RIU}$ . This complementary sensitivity profile between the two modes establishes an ideal platform for developing a dual-parameter sensing system capable of simultaneously monitoring both refractive index variations and temperature changes. These results highlight the correlation between mode field distribution characteristics and sensing sensitivity performance, and enabling high Q-factor dual-parameter sensing with potential applications in lab-on-a-chip systems and real-time biomolecular monitoring.

**Keywords:** dual-parameter sensing; bound states in the continuum; high Q-factor



Received: 18 April 2025 Revised: 27 May 2025 Accepted: 28 May 2025 Published: 30 May 2025

Citation: Liu, H.; Pan, Y.; Lu, H.; Chen, Z.; Huang, X.; Yu, C. High-Q Resonances Enabled by Bound States in the Continuum for a Dual-Parameter Optical Sensing. *Photonics* **2025**, *12*, 554. https://doi.org/ 10.3390/photonics12060554

Copyright: © 2025 by the authors. Licensee MDPI, Basel, Switzerland. This article is an open access article distributed under the terms and conditions of the Creative Commons Attribution (CC BY) license (https://creativecommons.org/licenses/by/4.0/).

## 1. Introduction

Optical sensing technology has garnered significant attention and widespread application in recent years, particularly in the fields of refractive index sensing and temperature sensing. Refractive index sensing holds substantial value in biomedical detection, environmental monitoring, and chemical analysis, while temperature sensing plays a critical role in industrial process control, energy management, and medical diagnostics [1–3]. Fiber optic sensing technology, owing to its high sensitivity, immunity to electromagnetic interference, and ease of integration, has become a key research direction in the field of optical sensing. Among these, fiber Bragg gratings (FBGs) and surface plasmon resonance (SPR) are two prominent fiber optic sensing technologies. FBGs detect changes in the external environment by reflecting light at specific wavelengths and are widely used in strain, temperature,

and refractive index sensing [4–6]. SPR, on the other hand, leverages the collective oscillation of free electrons on metal surfaces to achieve highly sensitive refractive index sensing, particularly excelling in biomolecular detection [7–9]. Additionally, other optical sensors based on optical fibers, such as long-period fiber gratings (LPFGs) and micro/nano fiber sensors, have demonstrated an excellent performance in refractive index and temperature sensing [10–14].

In recent years, bound states in the continuum, an emerging optical phenomenon, have attracted widespread attention from researchers. A BIC is a localized state embedded within a radiation continuum, characterized by an infinite Q-factor and exceptional light field localization capabilities [15–17]. BICs can be viewed as a special type of singularity that typically possesses topological properties [18]. Initially proposed in quantum mechanics, BICs have been experimentally demonstrated in optical structures such as photonic crystals (PhCs), metasurfaces, and waveguides [19–21]. Further, BICs in one-dimensional gratings have also been widely researched [22–24], which can be engineered under asymmetric conditions by adjusting the grating's period, duty cycle, or material refractive index.

Since BICs exhibit no far-field radiation and cannot be directly observed, slight structural asymmetry is typically introduced to transform the ideal BIC with an infinite Q-factor into a quasi-BICs with an ultrahigh Q-factor, enabling numerical simulations and experimental characterization. Owing to their unique properties, quasi-BICs have demonstrated significant potential in lasers, nonlinear optics, and sensing applications [25–27].

The application of quasi-BICs to optical refractive index and temperature sensing has become a research hotspot in recent years [28-30]. Quasi-BICs suppress radiative losses through structural symmetry or topological protection, theoretically achieving near-infinite Q-factors. The sensitivity of traditional SPR sensing depends on the evanescent field on the metal surface, with a penetration depth of approximately 100-200 nm. It can only detect molecules near the surface. In contrast, quasi-BIC confines the light field to subwavelength scales (such as nanoscale defects or gaps), resulting in an extremely high energy density. For example, in photonic crystal defects, the local volume of the light field can be 1–2 orders of magnitude smaller than the evanescent field of SPR, significantly enhancing the local electric field strength and, thus, improving the response to the adsorption of trace molecules, endowing quasi-BIC-based optical sensors with sensitivity far surpassing conventional SPR or micro-ring resonator sensors. Additionally, due to the optical field localization properties of quasi-BICs, quasi-BICs exhibit advantages over traditional optical sensing techniques in trace analyte detection and on-chip integration, demonstrating significant potential for the development of multifunctional integrated sensing platforms. By designing specific optical structures such as photonic crystal slabs or metasurfaces, BIC sensors enable highly sensitive refractive index and temperature detection with simplified optical configurations [31–37].

Recently, dual-mode effects in optical systems composed of microstructures are attracting increased research interest [38–40]. In this study, we designed and fabricated an all-dielectric transmission one-dimensional grating structure based on a silica substrate to enable a dual-mode system. The structure employs silicon as the dielectric layer, which can be patterned with sub-wavelength periodic features via electron beam lithography. A three-dimensional electromagnetic model was established using COMSOL 6.3 full wave simulation software. Periodic boundary conditions were applied to systematically investigate the electric field distribution characteristics and transmission spectral response of the grating. Simulation results revealed two resonant modes originating from BICs in the system. These two modes both exhibit typical symmetry-protected BICs, satisfying  $C_{2v}$  point group symmetry. Mode I achieves a refractive index sensitivity of  $S_{RI}^{\ \ I} = 406$  nm/RIU and a temperature sensitivity of  $S_T^{\ \ I} = 0.052$  nm/°C. For Mode II, the resonant wavelength

Photonics **2025**, 12, 554 3 of 12

exhibits a temperature sensitivity of  $S_{\rm T}{}^{\rm II}=0.078$  nm/°C (attributed to the thermo-optic effect of silicon) and a refractive index sensitivity of  $S_{\rm RI}{}^{\rm II}=220$  nm/RIU. By establishing a dual-mode collaborative detection matrix, the simultaneous measurement of the temperature and refractive index was realized. To validate the dual-parameter sensing potential of the grating, a dual-physical-parameter coupling model (temperature–refractive index) was developed.

# 2. Design of Dual-Mode Grating-Based Temperature—Refractive Index Sensor

The design of transmission grating sensor is illustrated in Figure 1. In this structure, silicon is chosen as the grating material due to its high thermo-optic coefficient and low fabrication cost, while a silicon dioxide ( $SiO_2$ ) layer serves as the substrate. Figure 1b details the unit cell structure of the grating, with a periodicity of P = 950 nm. Each unit consists of two infinitely long silicon bars and a bottom silicon slab. The silicon bars have a width of L1 = 200 nm, a height of h1 = 700 nm, and both silicon bars are centered at a distance of L2 = P/4 from the unit cell boundary, while the silicon slab exhibits a thickness of h2 = 70 nm. In simulations, the refractive index of the  $SiO_2$  substrate is set to 1.444.

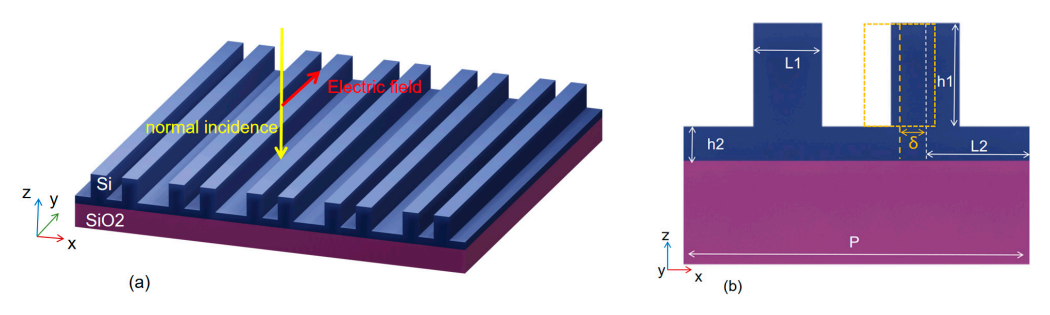


**Figure 1.** (a) Schematic diagram of the grating design. The grating employs a silicon dioxide (SiO<sub>2</sub>) substrate with silicon as the active medium. (b) Schematic of the unit cell structure. Each unit cell contains 2 silicon bars. Key geometric parameters are defined as: P = 950 nm, L1 = 200 nm, L2 = P/4, h1 = 700 nm, and h2 = 70 nm.

In this design, full-wave electromagnetic simulations of the grating structure are performed using COMSOL 6.3. The numerical analysis begins with calculating the transmission spectrum and electromagnetic field distribution under normal incidence when the grating is suspended in air. The grating structure, consisting of infinitely long silicon bars aligned along the y-axis, is positioned in the X–Y plane. Periodic boundary conditions are applied to the unit cell boundaries, with the excitation plane wave (electric field amplitude set to 1 V/m) propagating along the z-axis under y-polarized illumination.

It should be noted that symmetry-protected BICs exhibit complete decoupling from radiative channels due to their inherent symmetry, resulting in zero radiation leakage and undetectability in far-field measurements. To facilitate experimental observation of these BICs, we intentionally introduce structural asymmetry by applying a minute lateral displacement ( $\delta$ ) to the right silicon bar within each unit cell, as illustrated in Figure 1b. This controlled symmetry breaking enables the conversion of ideal BICs into quasi-BIC resonances with finite Q-factors, thereby permitting their characterization through far-field detection.

The numerical simulations reveal two distinct resonance modes in the grating structure. As demonstrated in Figure 2a, the transmission spectrum of the symmetric structure ( $\delta$  = 0) exhibits no resonance. However, when structural asymmetry is introduced ( $\delta$  = 10 nm), two prominent resonance features emerge at 1494.5 nm and 1847.03 nm, both showing near-zero transmission amplitudes. This is one special property of quasi-BICs, whose existence strictly depends on symmetry breaking.

Photonics **2025**, 12, 554 4 of 12

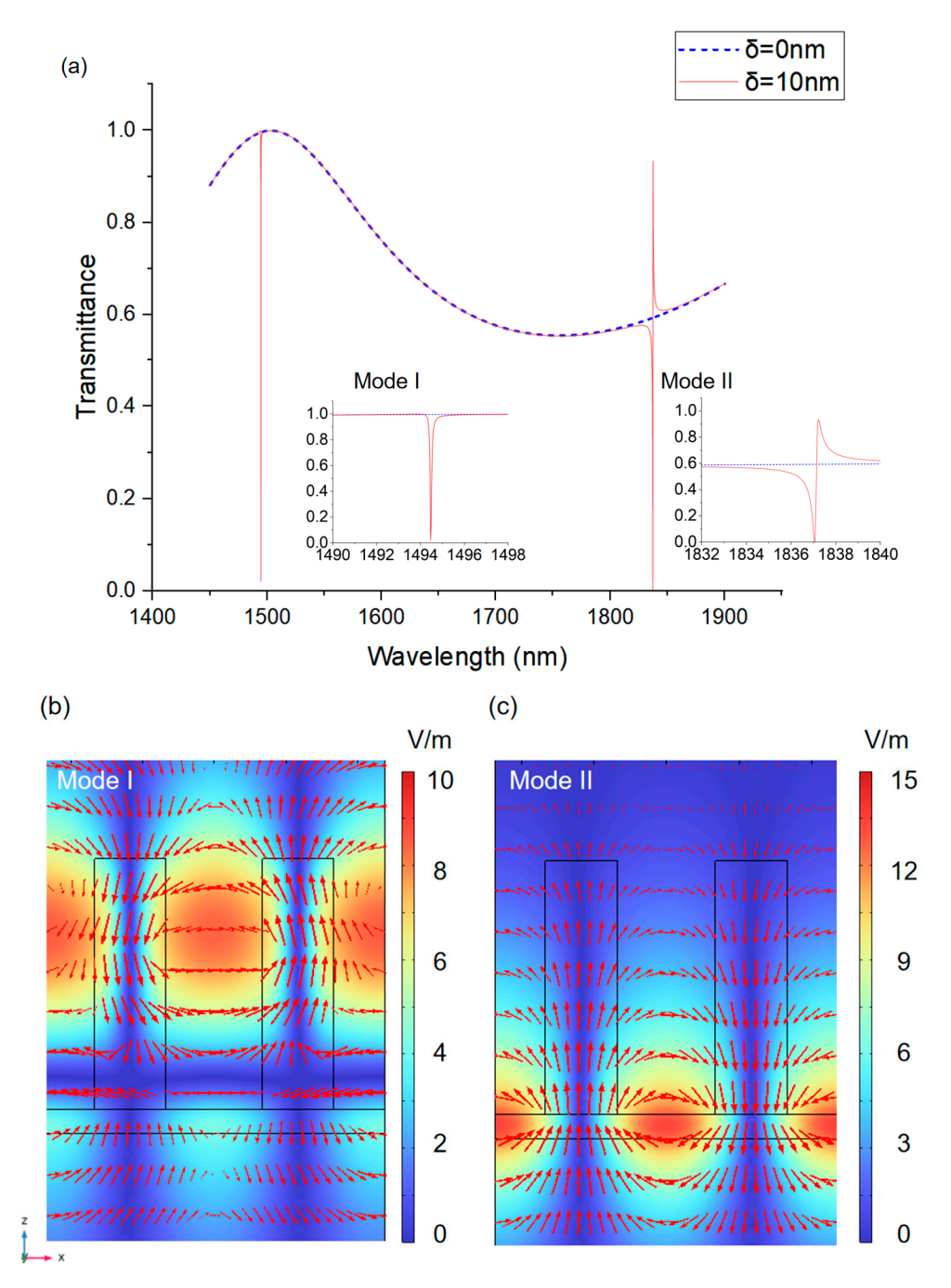
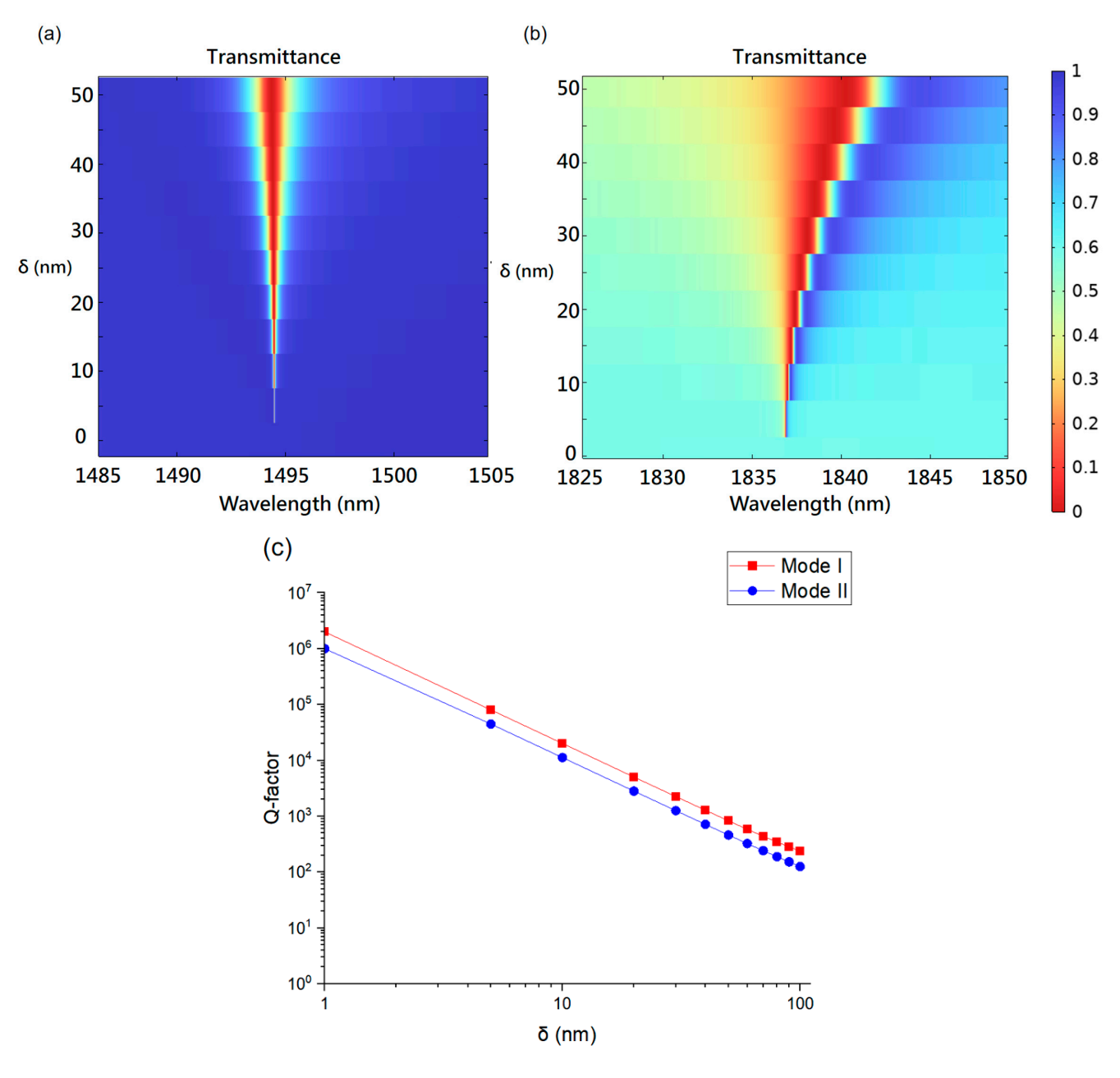


Figure 2. (a) The two spectral lines represent the transmission spectra of the grating structure with symmetry-breaking perturbation ( $\delta$  = 10 nm) and fully symmetric configuration ( $\delta$  = 0) in the 1400–1900 nm wavelength range when the environment temperature T = 20 °C and the refractive index n = 1.3. The red curve corresponds to the symmetry-broken structure, while the blue dash curve denotes the perfectly symmetric structure. The two inset figures show the spectra around Mode I and Mode II, respectively. (**b**,**c**) The electric field distribution (|E| component) of Mode I and Mode II, respectively. Both subfigures include color bars on the right for intensity scaling, with red arrows indicating the in-plane magnetic field directions.

Further, Figure 3a,b demonstrate the spectral evolution of Mode I and Mode II, respectively, under variations of the asymmetry parameter  $\delta$ . As  $\delta$  increases, both the resonance depth and resonance width of the spectra progressively enlarge. This behavior serves as direct evidence that the symmetry-protected BIC degenerates into a quasi-BIC with Fano-linearity upon symmetry breaking.

Photonics **2025**, 12, 554 5 of 12



**Figure 3.** (a,b) Transmittance spectrum of different  $\delta$  for Mode I and Mode II, respectively. The refractive index is set at n=1.3 and the temperature T=20 °C. The transmittance values are represented by color, with the corresponding color bar on the right for both figures. (c) Q-factor evolution of Mode I and Mode II as a function of  $\delta$ , with both axes plotted in logarithmic scale.

Further verification comes from the quality factor Q-factor dependence on asymmetry parameter  $\delta$ , as presented in Figure 3c. Both modes display characteristic BIC behavior with its Q-factor following an inverse quadratic dependence ( $Q \propto \delta^{-2}$ ), consistent with the theoretical framework of symmetry-protected BICs. When  $\delta$  is set to 5 nm, the Q-factor of both modes reach magnitudes on  $Q_{\rm I}=8.03\times10^4$  and  $Q_{\rm II}=4.48\times10^4$ , respectively. Further, as shown in Figure 2a, both modes exhibit extremely narrow bandwidths. Combined with the high Q-factors analyzed above, this grating demonstrates significant potential for sensing.

Figure 2b,c illustrate the electric field distributions of the two resonance modes, where color mapping represents the magnitude of the electric field intensity (|E|) and red arrows denote the in-plane magnetic field orientation. Mode I exhibits electromagnetic energy

Photonics **2025**, 12, 554 6 of 12

predominantly localized within the grating grooves, while Mode II shows strong field confinement in the silicon substrate. The spatially distinct distribution of this grating structure enables its potential for dual-parameter sensing: the groove-localized fields of Mode I render it highly responsive to ambient refractive index variations ( $\Delta n$ ) but minimally sensitive to temperature fluctuations ( $\Delta T$ ), whereas the silicon-confined fields of Mode II suppress refractive index sensitivity while amplifying thermo-optic responses due to silicon's high thermo-optic coefficient. This dual-mode configuration enables dual-parameter sensing through independent tracking of wavelength shifts, with orthogonal sensitivity profiles allowing for the simultaneous discrimination of the refractive index and temperature changes, thereby establishing the grating as a versatile photonic sensor.

## 3. Principle of Sensing and Discussion of Result

To enable simultaneous sensing of refractive index and temperature, we first construct a theoretical model based on the wavelength shift characteristics of quasi-BIC resonances. For one-dimensional grating, any resonance (including BICs) occurs only when the optical path length is an integer multiple of half the wavelength, as expressed by the following:

$$\frac{m\lambda_{resonance}}{2} = n_{eff}P \tag{1}$$

Here, P denotes the grating constant and m is an integer. The product of the effective refractive index  $n_{eff}$  and the grating period P equals the optical path length. The effective refractive index  $n_{eff}$ , governing light—matter interactions in the periodic structure, is defined as follows:

$$n_{eff} = \frac{k_{trans}}{k_0},\tag{2}$$

where  $k_0$  denotes the vacuum wave vector and  $k_{trans}$  represents the transverse wave vector governing mode propagation within the grating. From Equation (1), we observe a linear proportionality between resonance wavelength shifts ( $\Delta \lambda_{resonance}$ ) and variations in the effective refractive index ( $\Delta n_{eff}$ ). Furthermore, guided by effective medium theory, the field-dependent effective refractive index can be approximated using the following:

$$n_{\rm eff} \approx \sqrt{D \cdot n_{diel}^2 + (1-D) \cdot n^2},$$
 (3)

where D denotes the duty ratio of the grating medium (volume fraction occupied by dielectric), and  $n_{diel}$  and n represent the refractive indices of the grating material and groove-filling liquid, respectively. Based on this approximation formula, the effective refractive index  $n_{eff}$  exhibits a proportional relationship with  $n_{diel}$ . Consequently, quasi-BICs demonstrate linear wavelength shifts  $(\Delta \lambda_i)$ , where i serves as the mode identifier and (i = I,II) in response to refractive index variations  $(\Delta n_i)$  of the analytical solution, expressed as follows:

$$\Delta \lambda_i = k_i \cdot \Delta n_i \tag{4}$$

Furthermore, under moderate temperature variations where the thermo-optic coefficients ( $\alpha_i$ ) remains linear, we establish mode-specific relationships between refractive index changes and temperature fluctuations:

$$\Delta \lambda_i = \alpha_i \cdot \Delta T_i \tag{5}$$

When simultaneously considering temperature and refractive index variations, the wavelength shifts of both modes can be expressed as a linear superposition of thermo-optic

Photonics **2025**, 12, 554 7 of 12

effects and refractive-index-induced spectral displacements. This enables the establishment of a sensing matrix:

 $\begin{pmatrix} \Delta \lambda_{\rm I} \\ \Delta \lambda_{\rm II} \end{pmatrix} = \begin{pmatrix} s_{\rm RI}{}^{\rm I} & s_{\rm T}{}^{\rm I} \\ s_{\rm RI}{}^{\rm II} & s_{\rm T}{}^{\rm II} \end{pmatrix} \begin{pmatrix} \Delta n \\ \Delta T \end{pmatrix} \tag{6}$ 

where  $s_{\text{RI}}{}^i$  and  $s_{\text{T}}{}^i$  denote the refractive index and temperature sensitivity coefficients for Mode i (i = I, II), respectively. The non-singularity of this sensitivity matrix ( $Det(S) \neq 0$ ) guarantees the feasibility of simultaneous parameter discrimination through matrix inversion:

 $\begin{pmatrix} \Delta n \\ \Delta T \end{pmatrix} = S^{-1} \begin{pmatrix} \Delta \lambda_{\rm I} \\ \Delta \lambda_{\rm II} \end{pmatrix}. \tag{7}$ 

Next, the refractive indices of the two modes under different refractive index solutions and different temperatures were calculated separately through full-wave simulation. Figure 4a,b shows the transmission spectra near two modes' resonant points at refractive indices of 1.3, 1.31, 1.32, 1.33, 1.34, and 1.35 when the temperature is T = 20 °C, while Figure 4c,d presents the spectral lines at temperatures of 20 °C, 30 °C, 40 °C, 50 °C, and 60 °C when the refractive index n = 1.3. The spectral resolution of the full-wave simulation was set to 0.02 nm and the asymmetric parameter was set at  $\delta = 5$  nm.

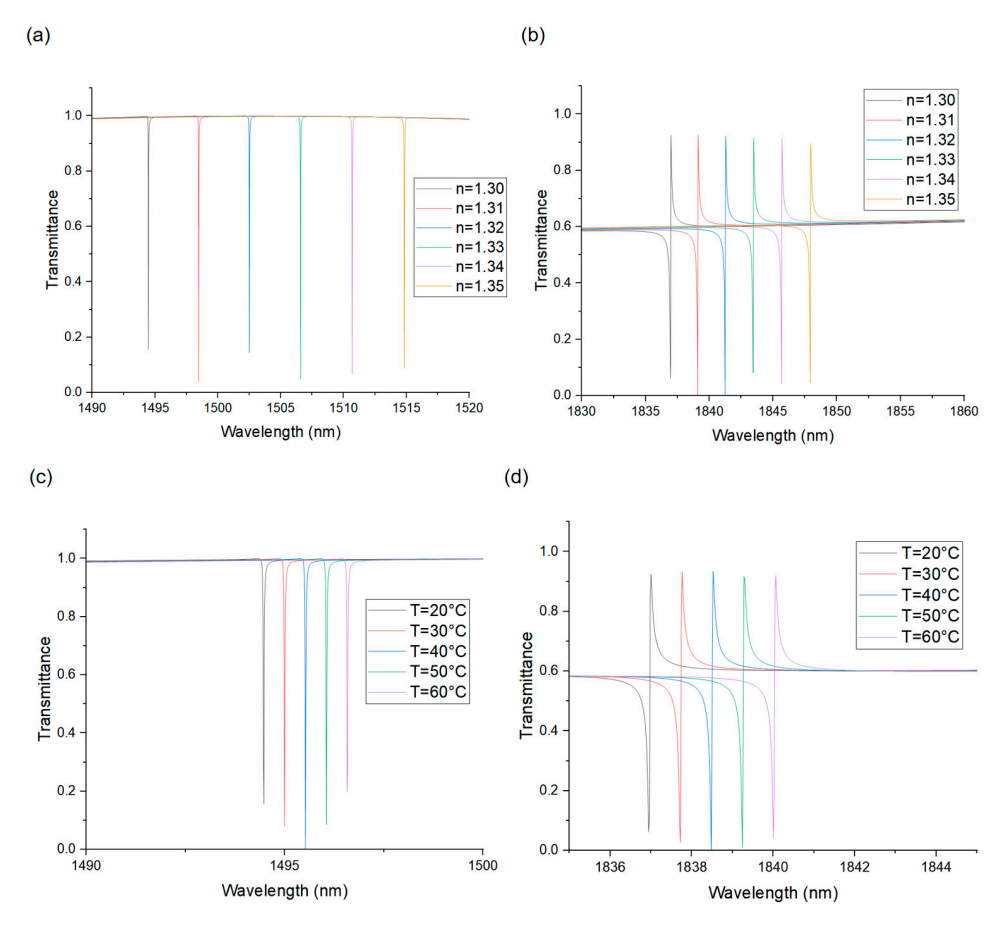


**Figure 4.** (**a**,**b**) The transmission spectra near Mode I and Mode II resonant point under different solution refractive indices when temperature T = 20 °C. (**c**,**d**) The transmission spectra near Mode I and Mode II at varying temperatures when the refractive index n = 1.3.

Through analysis of the transmission spectra, we extracted wavelength shifts of resonance points corresponding to the refractive index and temperature variations, with fitted curves presented in Figure 5. Specifically, Figure 5a quantifies the relationship between solution refractive index changes and wavelength shifts using 1.3 as the reference

Photonics **2025**, 12, 554 8 of 12

refractive index, while Figure 5b establishes the correlation between temperature variations and wavelength displacements with 20  $^{\circ}$ C as the reference temperature.

From Figure 5, the slopes of the linear fittings (i.e., sensing sensitivities) can be determined. Specifically, Mode I and Mode II exhibit refractive index sensitivities of  $S_{\rm RI}^{\rm I}=406~{\rm nm/RIU}$  and  $S_{\rm RI}^{\rm II}=220~{\rm nm/RIU}$ , respectively, and temperature sensitivities of  $S_{\rm T}^{\rm I}=0.052~{\rm nm/^{\circ}C}$  and  $S_{\rm T}^{\rm II}=0.078~{\rm nm/^{\circ}C}$ , respectively. The results quantitatively demonstrate the potential of this grating for dual-parameter sensing: the field distribution significantly influences the refractive index sensitivity. When the field is primarily confined within the dielectric material, the temperature sensitivity becomes notably higher due to the material's high thermo-optic coefficient, while showing low responsiveness to changes in the solution's refractive index. Conversely, when the field concentrates in the grating grooves, the refractive index sensitivity is substantially enhanced. Table 1 presents a comparative analysis of the performance between the design proposed in this work and other recently reported BIC sensors working in the near-infrared (NIR) and visible light band. The comparison reveals that this study employs an extremely simple grating structure to achieve high Q-factor and high-sensitivity simultaneous sensing of both the temperature and refractive index.

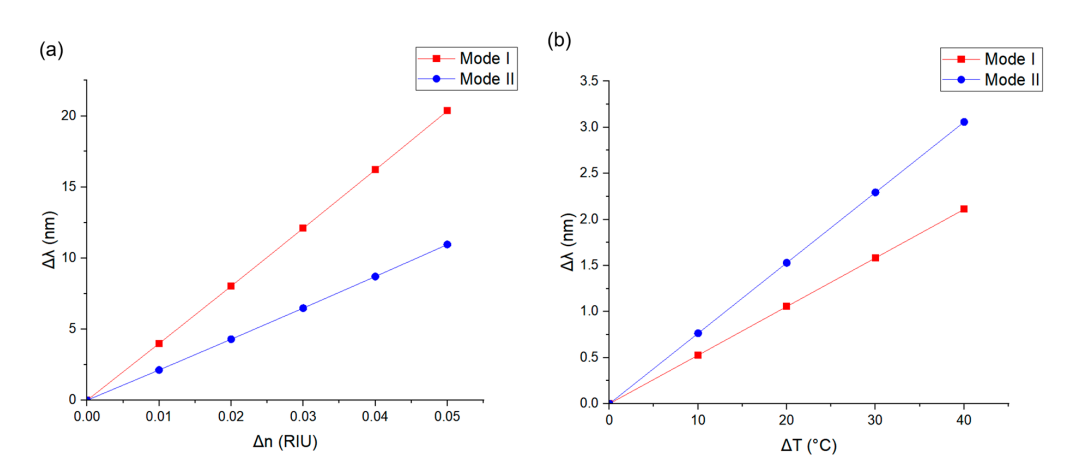


**Figure 5.** Wavelength shift versus (a) refractive index variation and (b) temperature.

**Table 1.** Performance comparison with different optical sensors based on BICs working in the NIR and visible band.

Ref.	Sensitivity of RI (nm/RIU)	Sensitivity of Temperature (nm/°C)	Capability for Dual-Parameter Sensing	Q Factor	Structure
Maksimov et al. [31]	137.2; 229.7	/	No	Not given	Silicon grating
Romano et al. [32]	4000	/	No	Not given	Silicon nitride PhC slab with nanoholes
Chen et al. [34]	122.2	/	No	415	Elliptic poly-Si nanopillars metasurface
Han et al. [35]	833; 1068	-0.043; -0.083	Yes	34,000; 160,000	Silicon PhC slab with nanoholes
Guo et al. [36]	746	0.054	No	54,757	Metasurface with split-disk unit
Zhao et al. [37]	262	0.0595	No	4225; 10,135	Metasurface with "H"-shaped disks and tilted gaps unit
This work	406; 220	0.052; 0.078	Yes	80,300; 44,800	Silicon grating and slab

Photonics **2025**, 12, 554 9 of 12

Substituting the sensitivities above into Equation (6) and taking the inverse matrix yields the following:

$$\begin{pmatrix} \Delta n \\ \Delta T \end{pmatrix} = \begin{pmatrix} 0.004 & -0.0029 \\ -11.3707 & 20.9841 \end{pmatrix} \begin{pmatrix} \Delta \lambda_{\rm I} \\ \Delta \lambda_{\rm II} \end{pmatrix}. \tag{8}$$

By utilizing the above formula, the temperature and refractive index of the solution being tested can be measured. The procedure involves two main steps: Firstly, measure the wavelengths of the two resonance modes in air at room temperature (20 °C). Secondly, measure the wavelengths of these two modes in the solution at a specific temperature. The wavelength differences  $\Delta\lambda_{I}$  and  $\Delta\lambda_{II}$  between the two modes can then be obtained by subtracting these measured values. Finally, by substituting these wavelength differences into Equation (8), both the refractive index and temperature of the solution can be determined.

#### 4. Uncertainty Evaluation

By using the eigenfrequency research module in COMSOL, the eigenfrequencies corresponding to different modes for each  $k_{\rm x}$  are calculated, as shown in Figure 6a,b, which illustrate that both Mode I and Mode II exhibit slight downward bending, indicating that oblique incidence induces a blue shift in the resonant wavelength, thereby influencing the sensing results. Therefore, it is essential to investigate the errors introduced by oblique incidence in sensing applications.

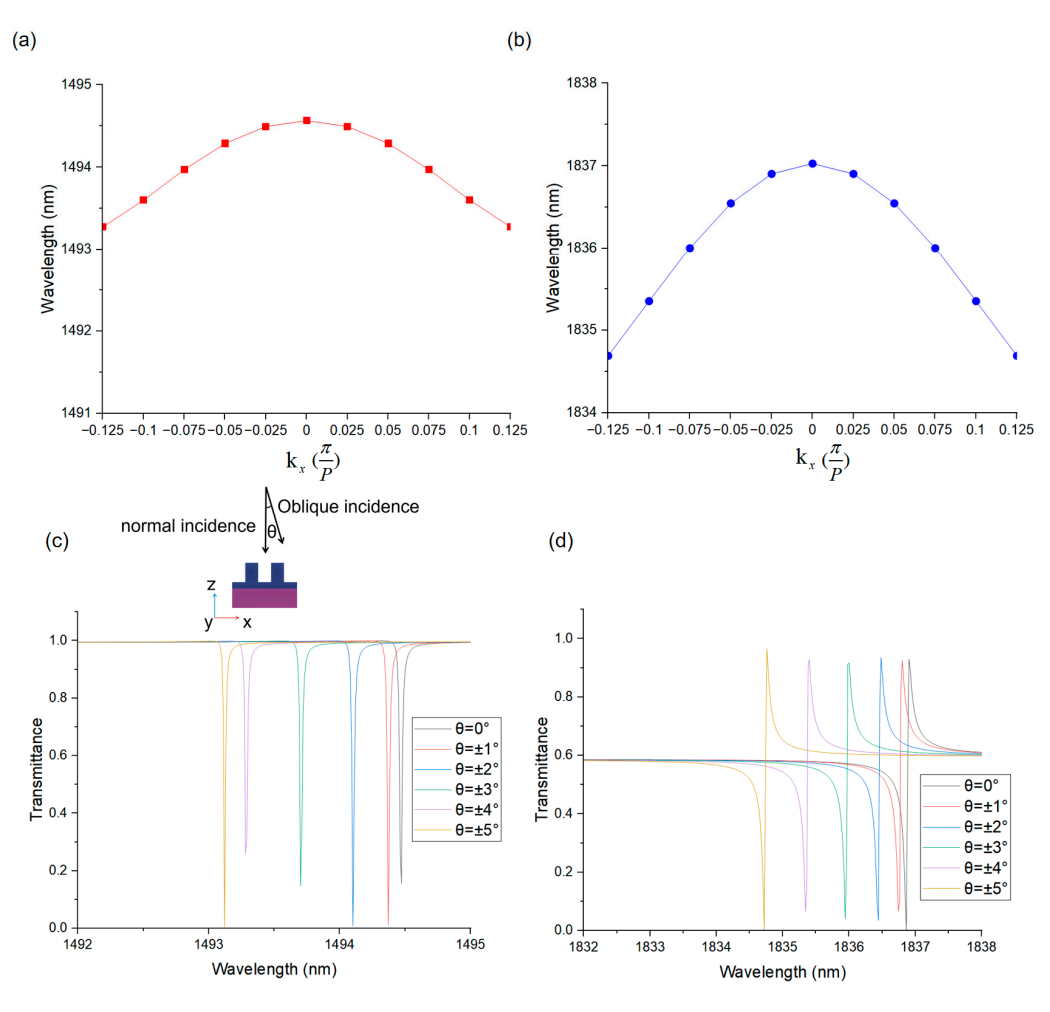


**Figure 6.** (**a**,**b**) The band diagrams of Mode I and Mode II within the  $(-0.125\pi/P, 0.125\pi/P)$  range. Wavelength shift for (**c**) Mode I and (**d**) Mode II with different incidence angles with a refractive index n = 1.3 and environment temperature T = 20 °C. The asymmetric parameter is set at  $\delta = 5$  nm.

Figure 6c,d illustrate the spectra near the frequency bands of the two modes under different oblique incidence angles. A  $5^{\circ}$  oblique incidence induces approximately 1.4 nm blue shift for Mode I and 2.2 nm blue shift for Mode II. Considering the orders of magnitude of sensitivity for temperature and refractive index sensing, it is evident that oblique incidence has a minor impact on the accuracy of refractive index sensing. However, for temperature sensing, oblique incidence introduces significant errors. As shown by the data in the figure combined with the temperature sensitivity calculated in the previous section, a mere  $1^{\circ}$  oblique incidence introduces temperature measurement errors of -1.9 °C and -2.5 °C. Therefore, it is critical to ensure that the laser is normally incident on the grating during sensing measurements to achieve the correct sensing result.

#### 5. Conclusions

This study demonstrates a breakthrough in optical sensing through dual-mode alldielectric transmissive grating. By engineering a silicon-on-silica grating, we achieved two quasi-BICs, exhibiting tunable high Q-factors ( $Q \propto \delta^{-2}$ ) under controlled asymmetry, enabling temperature sensing with sensitivities of  $S_{RI}^{I} = 406 \text{ nm/RIU}, S_{T}^{I} = 0.052 \text{ nm/}^{\circ}\text{C}$ for Mode I and  $S_{RI}^{II} = 220 \text{ nm}/\text{RIU}$ ,  $S_{T}^{II} = 0.078 \text{ nm}/^{\circ}\text{C}$  for Mode II. Additionally, the synergistic interaction of two resonant modes enabled the concurrent detection of the temperature and refractive index through a coordinated dual-parameter sensing matrix. This study not only investigates the impact of the mode field distribution on the sensing sensitivity, but also paves the way for scalable, lab-on-a-chip biosensors capable of real-time biomolecular analysis and environmental diagnostics. Future efforts will focus on experimental validation and integration with microfluidic systems to unlock real-world applications. Furthermore, this architecture can be integrated with active metadevices [41,42]—for instance, by adopting high electro-optic coefficient materials such as lithium niobate (LiNbO<sub>3</sub>) or potassium titanyl phosphate (KTP)—to enable real-time reconfiguration of resonance modes via external voltage control. This dynamic tuning capability allows for adaptive adjustment of the sensing sensitivity, on-demand spectral tailoring, and enhanced environmental feedback mechanisms.

**Author Contributions:** Conceptualization, H.L. (Hongshun Liu) and X.H.; methodology, H.L. (Hongshun Liu), H.L. (Hongshun Liu), and Z.C.; software, H.L. (Hongshun Liu) and Y.P.; writing—original draft preparation, H.L. (Hongshun Liu); supervision, X.H. and C.Y.; funding acquisition, C.Y. All authors have read and agreed to the published version of the manuscript.

**Funding:** The research was sponsored by Hong Kong Research Grants Council General Research Fund (15236424).

**Institutional Review Board Statement:** Not applicable.

**Informed Consent Statement:** Not applicable.

**Data Availability Statement:** The original contributions presented in this study are included in the article. Further inquiries can be directed to the corresponding author.

Conflicts of Interest: The authors declare no conflicts of interest.

#### References

- 1. Rao, Y.-J. In-fibre Bragg grating sensors. Meas. Sci. Technol. 1997, 8, 355. [CrossRef]
- Homola, J. Surface plasmon resonance sensors for detection of chemical and biological species. Chem. Rev. 2008, 108, 462–493.
   [CrossRef] [PubMed]
- 3. Lee, B.; Roh, S.; Park, J. Current status of micro-and nano-structured optical fiber sensors. *Opt. Fiber Technol.* **2009**, *15*, 209–221. [CrossRef]

4. Kersey, A.D.; Davis, M.A.; Patrick, H.J.; LeBlanc, M.; Koo, K.P.; Askins, C.G.; Putnam, M.A.; Friebele, E.J. Fiber grating sensors. *J. Light. Technol.* **1997**, *15*, 1442–1463. [CrossRef]

- 5. Erdogan, T. Fiber grating spectra. J. Light. Technol. 2002, 15, 1277–1294. [CrossRef]
- 6. Leng, J.; Asundi, A. Structural health monitoring of smart composite materials by using EFPI and FBG sensors. *Sens. Actuators A Phys.* **2003**, *103*, 330–340. [CrossRef]
- 7. Homola, J.; Dostalek, J.; Chen, S.; Rasooly, A.; Jiang, S.; Yee, S.S. Spectral surface plasmon resonance biosensor for detection of staphylococcal enterotoxin B in milk. *Int. J. Food Microbiol.* **2002**, *75*, 61–69. [CrossRef]
- 8. Kretschmann, E.; Raether, H. Radiative decay of non radiative surface plasmons excited by light. *Z. Für Naturforschung A* **1968**, 23, 2135–2136. [CrossRef]
- 9. Otto, A. Excitation of nonradiative surface plasma waves in silver by the method of frustrated total reflection. *Z. Für Phys. A Hadron. Nucl.* **1968**, 216, 398–410. [CrossRef]
- 10. Brambilla, G. Optical fibre nanowires and microwires: A review. J. Opt. 2010, 12, 043001. [CrossRef]
- 11. Fan, X.; White, I.M.; Shopova, S.I.; Zhu, H.; Suter, J.D.; Sun, Y. Sensitive optical biosensors for unlabeled targets: A review. *Anal. Chim. Acta* **2008**, 620, 8–26. [CrossRef]
- 12. Monat, C.; Grillet, C.; Collins, M.; Clark, A.; Schroeder, J.; Xiong, C.; Li, J.; O'Faolain, L.; Krauss, T.F.; Eggleton, B.J. Integrated optical auto-correlator based on third-harmonic generation in a silicon photonic crystal waveguide. *Nat. Commun.* **2014**, *5*, 3246. [CrossRef]
- 13. Shu, X.; Zhang, L.; Bennion, I. Sensitivity characteristics of long-period fiber gratings. J. Light. Technol. 2002, 20, 255.
- 14. Vengsarkar, A.M.; Lemaire, P.J.; Judkins, J.B.; Bhatia, V.; Erdogan, T.; Sipe, J.E. Long-period fiber gratings as band-rejection filters. *J. Light. Technol.* **1996**, *14*, 58–65. [CrossRef]
- 15. Hsu, C.W.; Zhen, B.; Stone, A.D.; Joannopoulos, J.; Soljačić, M. Bound states in the continuum. *Nat. Rev. Mater.* **2016**, *1*, 16048. [CrossRef]
- 16. Koshelev, K.; Lepeshov, S.; Liu, M.; Bogdanov, A.; Kivshar, Y. Asymmetric metasurfaces with high-Q resonances governed by bound states in the continuum. *Phys. Rev. Lett.* **2018**, *121*, 193903. [CrossRef] [PubMed]
- 17. Saad-Bin-Alam, M.; Reshef, O.; Mamchur, Y.; Carlow, G.; Sullivan, B.; Ménard, J.-M.; Huttunen, M.J.; Dolgaleva, K.; Boyd, R.W. Ultra-High-Q Resonance in a Plasmonic Metasurface. In Proceedings of the Conference on Lasers and Electro-Optics, Washington, DC, USA, 10–15 May 2020; p. FF3E.3.
- 18. Li, T.; Liu, M.; Hou, J.; Yang, X.; Wang, S.; Zhu, S.; Tsai, D.P.; Wang, Z. Chip-scale metaphotonic singularities: Topological, dynamical, and practical aspects. *Chip* **2024**, *3*, 100109. [CrossRef]
- 19. Bulgakov, E.; Sadreev, A. Symmetry breaking in a T-shaped photonic waveguide coupled with two identical nonlinear cavities. *Phys. Rev. B—Condens. Matter Mater. Phys.* **2011**, *84*, 155304. [CrossRef]
- 20. Friedrich, H.; Wintgen, D. Interfering resonances and bound states in the continuum. Phys. Rev. A 1985, 32, 3231. [CrossRef]
- 21. Marinica, D.C.; Borisov, A.G.; Shabanov, S.V. Bound states in the continuum in photonics. *Phys. Rev. Lett.* **2008**, *100*, 183902. [CrossRef]
- 22. Ning, T.; Li, X.; Zhao, Y.; Yin, L.; Huo, Y.; Zhao, L.; Yue, Q. Giant enhancement of harmonic generation in all-dielectric resonant waveguide gratings of quasi-bound states in the continuum. *Opt. Express* **2020**, *28*, 34024–34034. [CrossRef] [PubMed]
- 23. Wu, F.; Qi, X.; Qin, M.; Luo, M.; Long, Y.; Wu, J.; Sun, Y.; Jiang, H.; Liu, T.; Xiao, S.; et al. Momentum mismatch driven bound states in the continuum and ellipsometric phase singularities. *Phys. Rev. B* **2024**, *109*, 085436. [CrossRef]
- 24. Wu, F.; Wu, J.; Guo, Z.; Jiang, H.; Sun, Y.; Li, Y.; Ren, J.; Chen, H. Giant Enhancement of the Goos-Hänchen Shift Assisted by Quasibound States in the Continuum. *Phys. Rev. Appl.* **2019**, *12*, 014028. [CrossRef]
- 25. Kodigala, A.; Lepetit, T.; Gu, Q.; Bahari, B.; Fainman, Y.; Kanté, B. Lasing action from photonic bound states in continuum. *Nature* **2017**, *541*, 196–199. [CrossRef]
- 26. Liu, Z.; Xu, Y.; Lin, Y.; Xiang, J.; Feng, T.; Cao, Q.; Li, J.; Lan, S.; Liu, J. High-Q quasibound states in the continuum for nonlinear metasurfaces. *Phys. Rev. Lett.* **2019**, 123, 253901. [CrossRef]
- 27. Tan, T.C.; Srivastava, Y.K.; Ako, R.T.; Wang, W.; Bhaskaran, M.; Sriram, S.; Al-Naib, I.; Plum, E.; Singh, R. Active control of nanodielectric-induced THz quasi-BIC in flexible metasurfaces: A platform for modulation and sensing. *Adv. Mater.* **2021**, *33*, 2100836. [CrossRef] [PubMed]
- 28. Chen, R.; Li, T.; Bi, Q.; Wang, S.; Zhu, S.; Wang, Z. Quasi-bound states in the continuum-based switchable light-field manipulator. *Opt. Mater. Express* **2022**, *12*, 1232–1241. [CrossRef]
- 29. Fan, J.; Zhou, Y.; Xue, Z.; Xu, G.; Chen, J.; Xing, H.; Lu, D.; Cong, L. Active Singularity Metadevices Enabled by Bound States in the Continuum. *Laser Photon. Rev.* **2025**, 2401869. [CrossRef]
- 30. Li, N.; Chen, H.; Zhao, Y.; Wang, Y.; Su, Z.; Liu, Y.; Huang, L. Ultrasensitive metasurface sensor based on quasi-bound states in the continuum. *Nanophotonics* **2025**, *14*, 485–494. [CrossRef]
- 31. Maksimov, D.N.; Gerasimov, V.S.; Romano, S.; Polyutov, S.P. Refractive index sensing with optical bound states in the continuum. *Opt. Express* **2020**, *28*, 38907–38916. [CrossRef]

32. Romano, S.; Zito, G.; Lara Yépez, S.N.; Cabrini, S.; Penzo, E.; Coppola, G.; Rendina, I.; Mocellaark, V. Tuning the exponential sensitivity of a bound-state-in-continuum optical sensor. *Opt. Express* **2019**, 27, 18776–18786. [CrossRef] [PubMed]

- 33. Srivastava, Y.K.; Ako, R.T.; Gupta, M.; Bhaskaran, M.; Sriram, S.; Singh, R. Terahertz sensing of 7 nm dielectric film with bound states in the continuum metasurfaces. *Appl. Phys. Lett.* **2019**, *115*, 151105. [CrossRef]
- 34. Chen, W.; Li, M.; Zhang, W.; Chen, Y. Dual-resonance sensing for environmental refractive index based on quasi-BIC states in all-dielectric metasurface. *Nanophotonics* **2023**, *12*, 1147–1157. [CrossRef] [PubMed]
- 35. Han, Z.; Sun, F.; Wang, J.; Liu, Y.; Tian, H. Design and Theoretical Analysis of a Low Demodulation Deviation PhC Dual-Parameter Sensor Based on Quasi-BIC and Guided Mode Resonance. *IEEE Sens. J.* **2024**, 24, 29841–29850. [CrossRef]
- 36. Guo, L.; Zhang, Z.; Xie, Q.; Li, W.; Xia, F.; Wang, M.; Feng, H.; You, C.; Yun, M. Toroidal dipole bound states in the continuum in all-dielectric metasurface for high-performance refractive index and temperature sensing. *Appl. Surf. Sci.* **2023**, *615*, 156408. [CrossRef]
- 37. Zhao, J.; Fan, X.; Fang, W.; Xiao, W.; Sun, F.; Li, C.; Wei, X.; Tao, J.; Wang, Y.; Kumar, S. High-Performance Refractive Index and Temperature Sensing Based on Toroidal Dipole in All-Dielectric Metasurface. *Sensors* **2024**, 24, 3943. [CrossRef]
- 38. Chen, R.; Bi, Q.; Li, T.; Wang, S.; Zhu, S.; Wang, Z. Dual-wavelength chiral metasurfaces based on quasi-bound states in the continuum. *J. Opt.* **2023**, *25*, 045001. [CrossRef]
- 39. Li, T.; Liu, M.; Qin, J.; Ren, J.; Hou, J.; Liu, Y.; Yang, X.; Chu, H.; Lai, Y.; Wang, S.; et al. Configurable Topological Photonic Polycrystal Based on a Synthetic Hybrid Dimension. *Natl. Sci. Rev.* **2025**, nwaf107. [CrossRef]
- 40. Li, T.; Xu, X.; Fu, B.; Wang, S.; Li, B.; Wang, Z.; Zhu, S. Integrating the optical tweezers and spanner onto an individual single-layer metasurface. *Photon. Res.* **2021**, *9*, 1062–1068. [CrossRef]
- 41. Li, T.; Kingsley-Smith, J.J.; Hu, Y.; Xu, X.; Yan, S.; Wang, S.; Yao, B.; Wang, Z.; Zhu, S. Reversible lateral optical force on phase-gradient metasurfaces for full control of metavehicles. *Opt. Lett.* **2023**, *48*, 255–258. [CrossRef]
- 42. Li, T.; Xu, H.; Panmai, M.; Shao, T.; Gao, G.; Xu, F.; Hu, G.; Wang, S.; Wang, Z.; Zhu, S. Ultrafast Metaphotonics. *Ultrafast Metaphotonics* **2024**, *4*, 0074. [CrossRef]

**Disclaimer/Publisher's Note:** The statements, opinions and data contained in all publications are solely those of the individual author(s) and contributor(s) and not of MDPI and/or the editor(s). MDPI and/or the editor(s) disclaim responsibility for any injury to people or property resulting from any ideas, methods, instructions or products referred to in the content.